Marquar, W.; Raseale, S.; Prieto González, G.; Zimina, A.; Bikash Sarma, B.; Grunwaldt, J.; Claeys, M.... (2021). CO2 Reduction over Mo2C-Based Catalysts. ACS Catalysis. 11(3):1624-1639. https://doi.org/10.1021/acscatal.0c05019

CO_2 reduction over Mo_2C-based catalysts

Wijnand Marquart,[a] Shaine Raseale,[a] Gonzalo Prieto,[b] Anna Zimina,[c, d] Bidyut Bikash Sarma,[c] Jan-Dierk Grunwaldt,[c,d] Michael Claeys[a] and Nico Fischer[a]*

[a] Catalysis Institute and c*change (DST-NRF Centre of Excellence in Catalysis), Department of Chemical Engineering, University of Cape Town, Private Bag X3, Rondebosch 7701, South Africa.

[b] ITQ Instituto de Tecnología Química, Universitat Politècnica de València-Consejo Superior de Investigaciones Científicas (UPV-CSIC), Avenida de los Naranjos s/n, Valencia, 46022, Spain.

[c] Karlsruhe Institute of Technology, Institute of Catalysis Research and Technology (IFKT), Hermann-von-Helmholtz-Platz 1, Eggenstein-Leopoldshafen, 76344, Germany.

[d] Karlsruhe Institute of Technology, Institute for Chemical Technology and Polymer Chemistry (ITCP), Engesserstr. 20, Karlsruhe, 76131, Germany.

ABSTRACT: Four Mo-based catalysts were prepared via three different synthesis techniques supported on SiO_2 and/or SBA-15. By means of complementary *in situ* characterization techniques, the carburization process and the final characteristics of these catalysts were investigated. Additionally, the four catalysts were evaluated for the activation of CO_2 in the absence and presence of H_2 (reverse water-gas-shift, RWGS). The results suggest that CO_2 reacts via a dissociation on the carbide surface, forming adsorbed oxygen surface species. Severe oxidation of the carbide into its oxidic phases (MoO_2 or MoO_3) only occurs at temperatures above 850 K in the presence of CO_2. O_2 dissociates on the carbide surface when introduced at low concentrations (1 vol.%) at room temperature, but when exposed to higher concentrations a strong exothermic bulk re-oxidation reaction occurs, forming MoO_2. All four catalysts show high RWGS activity in terms of CO_2 conversions with a minimum CO selectivity of 98 % without any signs of bulk catalyst oxidation. Although minimal, the observed deactivation is suggested to be

primarily due to phase changes between Mo_2C allotropes (β-phase, oxycarbide and η-phase) and/or sintering of the active phase.

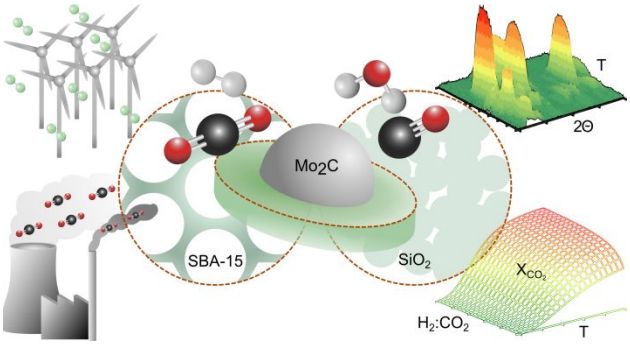

KEYWORDS: carbon dioxide, hydrogen, reverse water-gas-shift, molybdenum carbide, *in situ* XRD, *in situ* Raman spectroscopy, *in situ* XAS

INTRODUCTION

As one of the main causes for climate change and global warming, it is of upmost importance to reduce CO_2 emissions and its concentration in the atmosphere as fast as possible to realize the goal of the Paris Agreement limiting the global warming to below 2 K. It is generally agreed that 95 % of the observed climate change is a direct result of human activities causing an increase in concentration of anthropogenic greenhouse

gases in the atmosphere largely due to the burning of fossil fuels for power generation and large scale commercial chemical processes.[1,2]

Carbon capture and sequestration (CCS) or carbon capture and utilization (CCU) are the only methods to minimize concentrations in the atmosphere as well as emissions with the expected continued, albeit reduced, use of fossil fuels.[3] Possible ways to capture CO_2 is before it is emitted or directly from air.[4] These processes come with high capital and operational costs and it is therefore of great interest to investigate pathways to reduce costs, or to add value by producing commercial products such as synthetic fuels, building materials, chemicals and polymers from the captured CO_2. Multiple processes are reported and discussed for the conversion of CO_2 into commercial products, including catalytic, electro-chemical, mineralization, biological, photocatalytic and photosynthetic pathways.[3] To date, the largest commercial processes using CO_2 are the synthesis of urea (130 MT of CO_2 annually), the enhanced oil recovery (70-80 MT of CO_2 annually) and the methanol synthesis (2 MT of CO_2 annually) along with the food and beverage industry, cooling, fire suppression, metal fabrication and stimulating plant growth in greenhouses.[5,6] However, this is not nearly enough. China's 2017 CO_2 emissions due to

the combustion of coal, oil and natural gas alone were estimated at 9301 MT.[7] It is therefore evident that any pathway to convert CO_2 into value added product must not only be net CO_2 negative but also operate on world scale and produce base chemicals in large quantities to be able to affect the global emissions.

Other catalytic processes using and at least partially converting CO_2, which have gained interest in the past decades and are in various stages of development and commercialization, are the (in)direct CO_2 hydrogenation to fuels (such as the Air-to-fuels system from Carbon Engineering in Canada or INERATEC in Germany) and CO_2 dry-reforming of hydrocarbons (such as CO_2 dry reforming of methane by BASF SE & Linde in Germany).[8,9] In general, the challenge is to activate CO_2, which is thermodynamically low in energy and needs to be reacted with high energy molecules such as green hydrogen to hydrocarbons or oxygenates either in a single step or in multiple reactions. Assuming the availability of green hydrogen and cheap renewable energy in future, the reverse water-gas-shift reaction (RWGS), i.e. the reduction of CO_2 with H_2 to CO and water, will play a significant role in these processes.

The focus of this study is to utilize Mo_2C-based catalysts, synthesized using three different techniques, under reverse water-gas-shift conditions and to evaluate their performance varying reaction temperature, space velocity and feed gas composition (CO_2 to H_2 ratio). Mo_2C has been shown to be highly active for the activation of CO_2 in various processes.[10-13] While the RWGS reaction is endothermic, under similar process conditions the CO_2 methanation reaction, a possible side reaction, is an exothermic process. This means that high temperatures (above 900 K) are required for the RWGS reaction to become thermodynamically favored over the methanation pathway. The catalysts were prepared via three different synthesis techniques, of which two were adapted from Amrute et al.[14] and Han et al.[15], in order to study the effect the different routes have on the physical properties of Mo_xC_y such as crystal structure[16], crystallite size and surface area. In most literature reports, the beta-carbide is synthesized by a temperature programmed reaction, i.e. carburization treatment, of MoO_3 with a CH_4 in H_2 mixture yielding (hexagonal) β-Mo_2C, a method originally described by the research group of Boudart.[17] However, large differences in synthesis protocols, such as the molybdate salt precursor, the calcination temperature required to convert the precursor to MoO_x,

carburization temperature and carburizing gas composition (such as CO, CH_4:H_2, C_3H_8:H_2) are reported. Varying these parameters has most likely an impact on the physical properties of the materials and thus on the catalytic performance. In our previous study we have touched on the effect of carburization temperature on the transformation of bulk MoO_3 to β-Mo_2C, specifically focusing on carbon deposition.[18] In this study, using mainly supported Mo_xC_y catalysts obtained via different synthesis pathways, we perform a comprehensive investigation into the carburization process, CO_2 activation and RWGS activity focusing on the physical properties of the catalyst using *in situ* characterization techniques including X-ray diffraction (XRD), Raman spectroscopy and X-ray absorption spectroscopy (XAS).

THERMODYNAMICS

In an earlier study from our research group, an extended thermodynamic analysis was performed on the CO_2 assisted oxidative dehydrogenation of ethane and its relevant side reactions as a function of product species and reaction conditions.[19] Here we focused on the reverse water-gas-shift reaction and its prominent side reaction, the methanation of CO_2. When minimalizing the Gibbs free energy of the entire system as a function of

temperature with a feed ratio (H_2 : CO_2) of 1 and a pressure of 1 bar (see Figure 1-A), the thermodynamic analysis suggests that at lower temperatures (< 675 K) the reduction of CO_2 to H_2O and solid carbon (assumed as graphite) is the most favorable reaction. Simultaneously, at 675 K the methanation reaction is predicted to be at its maximum. CO starts to form as CH_4, C and H_2O contents drop, surpassing CH_4 concentrations at 800 K. Above 1025 K a H_2O to CO product ratio of 1 is observed, the desired product ratio for the RWGS. When increasing the H_2 to CO_2 ratio to 4 (see Figure 1-B), the stoichiometric composition of CO_2 methanation, at 300 K a stoichiometric H_2O to CH_4 product ratio of 2 is calculated. An increase in temperature is followed by a slight decrease in this ratio. CO is predicted to be formed from 700 K onwards, overtaking CH_4 at 900 K. A H_2O to CO ratio of 1 is observed from 1100 K. No formation of solid carbon is predicted over the entire temperature range.

It is also interesting to study the thermodynamic equilibrium conversion of all (side) reactions individually. The considered reactions are the reverse water-gas-shift (RWGS), methanation of CO_2 (MCO_2), methanation of CO (MCO), (reverse) Boudouard reaction (BR) and methane decomposition (MD) (see Figure 1-C). Note that the calculations do

not represent a mechanistic or pathway analysis. Since RWGS is an endothermic reaction, an increase in temperature increases its equilibrium conversion. Only above 900 K the RWGS reaction is thermodynamically more favorable than the two methanation reactions (MCO_2 & MCO). While the decomposition of CH_4 increases with temperature, increasing the possibility of solid carbon formation, so does the reverse Boudouard reaction, forming CO from CO_2 and solid carbon. To maximize the CO yield in the RWGS reaction, an effective catalyst therefore must kinetically hinder the methanation pathways without suppressing the CO_2 reduction.

In order to understand which process conditions are required to achieve the maximum possible CO_2 conversion in the RWGS and CO_2 methanation, the thermodynamic equilibrium conversion is computed as a function of temperature, feed ratio and dilution (the percentage of inert gas fed relative to the reactants), keeping in mind that the latter has no effect on the RWGS reaction. It is confirmed that higher temperatures and H_2 to CO_2 ratios yield higher CO_2 conversion in the RWGS (see Figure 1-D). However, a higher H_2 to CO_2 ratio also favors the CH_4 formation due to the increase in equilibrium conversion for the methanation reaction (see Figure S1).

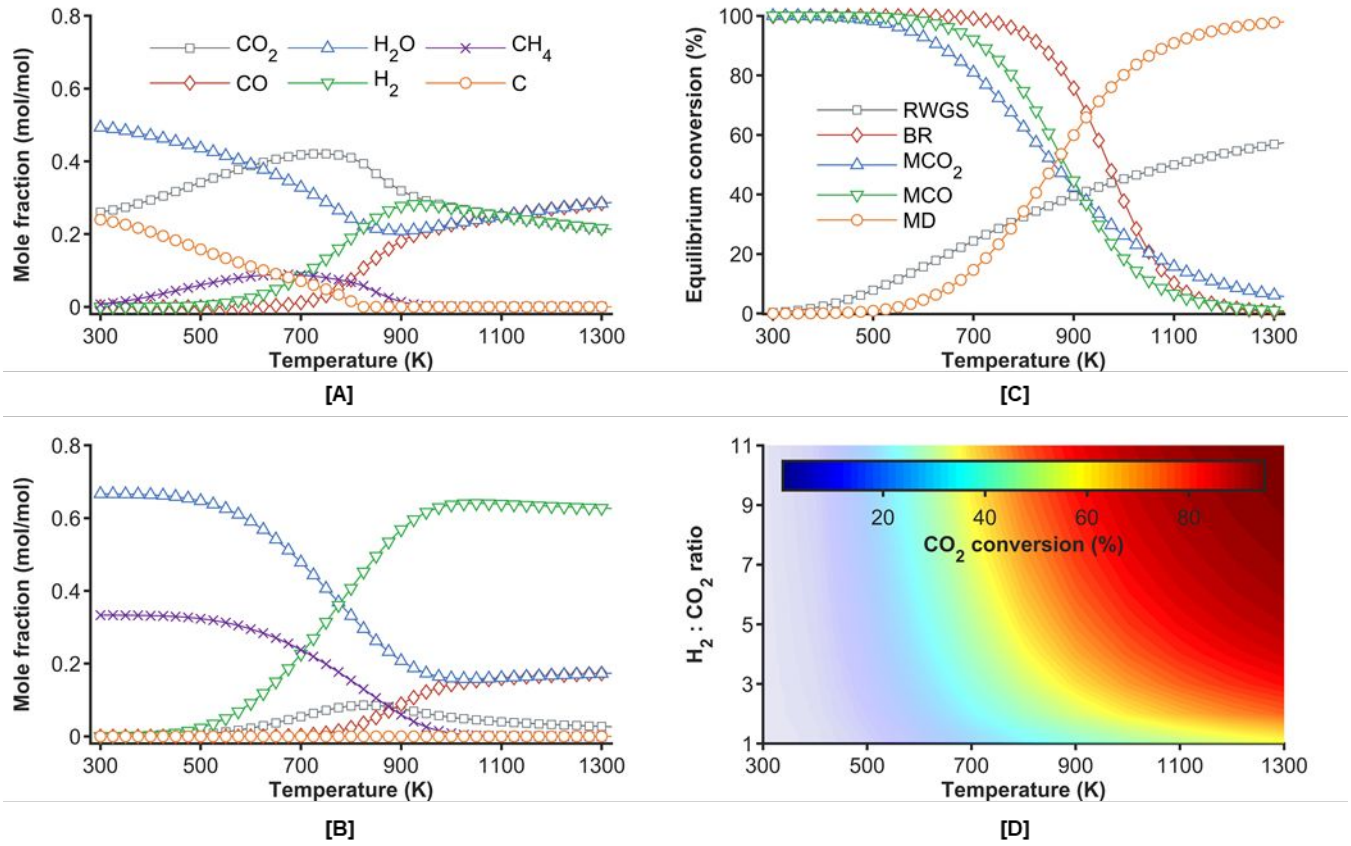

Figure 1. Thermodynamic prediction of the equilibrium composition as a function of temperature at **[A]** a H_2:CO_2 feed ratio of 1, at 1 bar pressure and **[B]** a H_2:CO_2 feed ratio of 4, at 1 bar pressure. **[C]** Individual equilibrium conversions as a function of temperature, stoichiometric feed and at 1 bar pressure. **[D]** Effect of feed ratio (H_2 to CO_2) and temperature on the equilibrium conversion of reverse water-gas-shift at 1 bar pressure. Compound specific thermodynamic parameters from Knacke et al.[20].

EXPERIMENTAL SECTION

Synthesis of Mo_2C/SiO_2-WI and Mo_2C/SBA-15-WI. The wet impregnation (WI) method was utilized. In a typical synthesis, per gram of support material (non-porous SiO_2 or meso-porous SBA-15), 10 ml of a 0.29 M aqueous solution of ammonium heptamolybdate (AHM, SAARCHEM PTY LTD, 81.5 % MoO_3) was added dropwise, yielding a Mo loading of 20 wt.-%. The suspension was stirred for 30 minutes. For the preparation of Mo_2C/SiO_2-WI, the batch size was increased to 100 ml of aqueous AHM and 10 g of SiO_2 (AEROSIL® 200). The sample was then dried by means of a rotary evaporator, using a round bottom 500 ml Büchi flask at 333 K, 72 mbar and 155 rpm. For Mo_2C/SBA-15-WI, the sample was dried in an oven at 393 K until a dry powder was obtained. The dried powder samples were loaded into a 1/4" quartz fixed bed reactor and carburized to Mo_2C in a temperature programmed reaction in a 20 vol.-% CH_4 in H_2 atmosphere.[17,21] The carburization temperature was optimized and all samples used for catalytic testing were carburized at 873 K with a ramp rate of 1 K/min, holding for 5 hours at maximum temperature under atmospheric pressure with a reactant flow rate of 250 ml/min·g_{cat}^{-1}. After completion of the carburization process, the catalyst was either passivated at room temperature (for

characterization purposes) in a flow of 1 vol.-% O_2 in N_2 for 1 hour (250 ml/min·g_{cat}^{-1}) or directly exposed to testing conditions.

Synthesis of Mo_2C/SiO_2-SG. The Sol-Gel (SG) method was adapted from Amrute et al.[14]. In short, 3.07 g of ammonium heptamolybdate was dissolved in 100 ml hot distilled water, targeting a final loading of 20 wt.-% Mo on SiO_2. The AHM solution was added dropwise under stirring to a solution of 37.16 ml tetraethyl orthosilicate (TEOS, Sigma-Aldrich, 99.99 %) in 20 ml 2-propanol (anhydrous, Sigma-Aldrich, 99.5 %), followed by a 3 hour ageing step while continuously stirring. The obtained greenish precipitate was further aged inside the flask for 2 days at room temperature (RT), resulting in a gel of the same color. The gel was dried in an oven at 393 K overnight followed by calcination in a Nabertherm calcination oven for 10 hours at 773 K in a stagnant air atmosphere. After calcination the obtained MoO_3 on SiO_2 is carburized at 873 K for 5 hours under atmospheric pressure in 250 ml/min·g_{cat}^{-1} of 20 vol.-% CH_4 in H_2. After completion of the carburization process, the catalyst was either passivated (for characterization purposes) in 1 vol.-% O_2 in N_2 for 1 hour (250 ml/min.g_{cat}^{-1}) or directly exposed to the required reaction conditions.

Synthesis of Mo_2C/SBA-15-HNC. The hybrid nanocrystal (HNC) synthesis technique was adapted from Han et al.[22]. For a typical synthesis, yielding a 20 wt.-% Mo loading, a 2.4 M hydrochloric acid (Kimix, 33 %) aqueous solution was added dropwise to 180 ml of 0.067 M aqueous sodium molybdate ($Na_2MoO_4 \cdot 2H_2O$, Sigma-Aldrich, ≥99.5 %) solution while monitoring the pH. At a pH of 4.5, 40 ml of 0.16 M cetyl trimethyl ammonium bromide (CTAB) aqueous solution (CTAB to Mo molar ratio of 0.53 : 1) was added dropwise, under vigorous stirring (>1000 rpm). After complete addition of CTAB, the pH was again adjusted to 4.5 by means of the HCl solution. The mixture was stirred for another 2 hours. After completion, the white suspension was transferred to an autoclave and exposed to a hydrothermal deposition treatment of the crystals onto previously prepared SBA-15 (synthesized with a method reported by Nair[23]). The autoclave was heated to 373 K while stirring (650 rpm) and held at that temperature for 12 hours. The mixture was washed with DI water, filtered using a Büchner funnel and dried in an oven overnight at 333 K. Once dry, the sample was calcined in a tubular furnace at 673 K (heating rate 5 K/min) for 5 hours under air flow (50 ml/min·g_{cat}^{-1}). The carburization took place using the same

method as above, at 873 K or 923 K for 5 hours under atmospheric pressure flowing 250 ml/min·g_{cat}^{-1} of 20 vol.-% CH_4 in H_2.

Catalyst characterization. *X-ray diffraction (XRD) analysis.* Offline XRD analysis was performed on the prepared and passivated samples to identify which of the different crystal allotropes of molybdenum is present. The diffraction patterns were compared to reference data files reported in a database (PDF-2, released in 2008 and PDF-4+, released in 2019). The diffraction patterns were acquired in the 2Θ range of 20° to 120° (1/d = 0.19 to 0.97 $Å^{-1}$) using a step size of 0.043° and with a time per step of 0.75 seconds. The total scan time amounts to 30 min, performed on a D8 Advance diffractometer (Bruker, Germany) equipped with a position-sensitive detector (LYNXEYE) in Bragg Brentano geometry. Power to the Co anode was set at 35 kV and 40 mA. Quantitative analysis was performed using the refinement method by Rietveld[24] utilizing the software package TOPAS 5 (Bruker AXS).

In situ X-ray diffraction analysis. Online XRD analysis was conducted using a XRK900 Anton Paar reaction cell attached to a laboratory XRD (Bruker D8 Advance) operated at 50 kV and 35 mA. The diffractometer was equipped with a molybdenum source and a

position sensitive detector (Bruker AXS Vantec). The scans were collected every 5 minutes in the 2Θ range of 10° to 28° (1/d = 0.25 to 0.65) at a step size of 0.017° and time per step of 0.2 sec. 150 mg of the powder samples, loaded in the flow through holder, were carburized using a diluted mixture of 20 vol.-% CH_4 in H_2 with an absolute H_2 content of 10 vol.% in N_2. A total flowrate of 100 ml/min was applied while ramping the temperature at 1 K/min to 873 K and held at 873 K for 5 h.

Raman spectroscopy. Raman spectra were collected using a Witec Confocal Raman Microscope Alpha300 and collected in the range of 3500 to 100 cm^{-1} using a 532 nm green laser under ambient conditions. The specific particles analyzed were targeted using a CCD camera connected to a Zeiss EC Epiplan-Neufluar 100x/0.9 objective. The spectra were taken using a laser power of 2.5 mW, an integration time of 1.2 seconds and 20 accumulations. The software package WITecProject (WITec, Germany) was used for the data analysis.

In situ Raman spectroscopy. 29 mg of powder sample were loaded on a P_{atm} Linkam cell using a 785 nm laser source for *in situ* studies (ITQ, Valencia). The cell was slightly modified to allow sample temperatures up to 873 K. For the *in situ* carburization treatment,

a total flow of 30 ml/min of the gas mixture (10 vol.-% CH_4, 40 vol.-% H_2, balance He) was established through the cell. Then the temperature was increased from RT to 873 K in 50 K steps (heating rate of 3 K/min between temperature levels) and the Raman spectra recorded *in situ* at each temperature.

Transmission Electron Microscopy (TEM) analysis. TEM micrographs of the samples were taken using a Tecnai F20 transmission electron microscope equipped with a field emission gun (operated at 200kV). The samples were prepared via suspension of a small volume of the materials in 100% ethanol. A droplet of the suspension was transferred onto a holey carbon-coated copper grid and air dried.

Inductively Coupled Plasma optical emission spectroscopy (ICP-OES). The elemental analysis was performed using a Varian 730 ES ICP-Optical Emission Spectrophotometer. The samples were digested with a Mars 6 Microwave digester using HNO_3 and HF for digestion and H_3BO_3 for neutralization.

Thermogravimetric analysis (TGA). The TGA experiments were performed in a Discovery SDT 650 instrument (TA instruments, USA). The sample loading, depending on the density of the sample, ranged between 5-30 mg of solid sample, which was placed

into an alumina pan in parallel with an empty reference pan. The carburization of the samples was performed using a diluted mixture of 20 vol.-% CH_4 in H_2 with an absolute H_2 content of 4 vol.-% in inert gas (Ar/N_2). A total flow of 100 ml/min with a temperature ramp from 323 K to 873 K at a rate of 1 K/min was applied.

X-ray absorption spectroscopy (XAS). Ex situ XAS transmission experiments were performed at the Diamond Light Source facility at the B18 general purpose XAS beamline as part of the Block Allocation Group of the UK Catalysis Hub in December 2018. The carburized samples were analyzed at the Mo K-edge including three reference materials prepared in our laboratories, MoO_2, MoO_3 and β-Mo_2C (see Figure S15). Each scan was repeated 3 times to increase statistical relevance. The samples were all pressed into pellets with cellulose prior to the analysis. Data processing was performed using Athena from the Demeter software package.[25] The linear combination fitting tool was applied for all samples with the three reference materials, for phase quantification.

In situ X-ray absorption spectroscopy. XAS analysis at Mo-K edge were performed at the CAT-ACT beamline[26] of the KIT synchrotron in Karlsruhe, Germany. The XAS data were recorded in transmission mode using the ionization chambers. The energy of

Si(311) double crystal monochromator was calibrated by setting the first maximum of the first derivative of the XAS spectrum measured on Mo foil to the tabulated value of 20.000 keV. Data analysis was performed using Athena from the Demeter software package.[25] All samples were pressed in pellets, crushed and sieved to 100-200 µm. *In situ* experiments were performed in quartz capillaries of 1.5 mm diameter (20 µm wall thickness) as reactor. The reactor was placed inside a newly build oven made with copper[27] and covered with the X-ray transpired Kapton windows. The heating was realized using the resistance wires around ceramic rods, which were in turn placed above and below the capillary; the temperature was monitored by the thermocouple inside the oven calibrated to the temperature inside the capillary prior to the experiment (accuracy better than ±10K at 1000 K). The samples were first exposed to a carburization treatment in 20 vol.-% CH_4 in H_2. Temperature was increased to 650 K with a linear ramp rate of 10 K/min, followed by a further ramp to 920 K with 2 K/min. The temperature was held at 920 K for 2.5 h before cooling down to room temperature. Subsequently, the gas mixture was changed to 1 % CO_2 in He. The temperature was increased to 600 K with 10 K/min followed by a ramp to 1010 K at 5 K/min. The temperature was held at 1010 K for 1 h

before the sample was cooled down to room temperature. The total gas flowrate of each experiment was 50 ml/min controlled by the mass flow controllers (Bronkhorst, Germany). The EXAFS data up to k = 16 $Å^{-1}$ were recorded at room temperature before the carburization, after the carburization and after the temperature programmed reaction (TPR) with CO_2. During the temperature-programmed reactions, rapid XANES spectra were measured (2 min per spectrum, from 19 900 to 20 400 eV) to follow the changes in the chemical state of Mo during the carburization and TPR in CO_2. The reference materials (commercial MoO_2 and in-house prepared MoO_3, β-Mo_2C and α-MoC_{1-x}, see Figure S15) were diluted with cellulose to about 20 vol.-% of Mo and pressed in pellets for the transmission measurements.

Catalyst testing. The evaluation of the catalysts' performance under CO_2 activation and reverse water-gas-shift conditions was conducted in a 1/4" quartz tubular fixed-bed reactor under atmospheric pressure. In general, after the carburization process had been completed, the catalyst was exposed to an argon flow (250 ml/min·g_{cat}^{-1}) creating an inert atmosphere while cooling down to reaction temperature (in the range of 673 K to 873 K). Once the target temperature was reached, the catalyst was exposed to the reactant feed

gas. For the CO_2 activation experiments a 1 vol.-% CO_2 in N_2 (SV = 60 L/h·g_{cat}^{-1}) was established and for RWGS a gas mixture containing a H_2 to CO_2 ratio in the range between 1 and 7 diluted in Ar (50 : 50 vol.%). The space velocity ranged between 60 L/h·g_{cat}^{-1} and 120 L/h·g_{cat}^{-1}. The product stream was analyzed online using an Agilent 490 micro gas chromatograph (GC) equipped with three thermal conductivity detectors (TCD), two molecular sieve 5Å PLOT columns of 10 and 20 m lengths and one 10 m PoraPlot Q column.

RESULTS AND DISCUSSION

Optimizing carburization protocols. All samples were prepared targeting a 20 wt.-% Mo loading on the support material (see Table S1 for ICP-OES results) with similar Mo_2C crystallite sizes, to minimize the variables resulting from the three different synthesis techniques. Two samples were prepared on a non-porous SiO_2 support (impregnation on AEROSIL® 200 and *in situ* generated SiO_2 from TEOS for Sol-Gel synthesis), while the other two are supported on previously prepared mesoporous silica, SBA-15. As observed during our previous study[18] and reported in literature[28], the carburization process can result in a significant amount of carbon deposited on the surface of the catalyst, which

affects the active surface area, by blocking active sites and decreasing the catalytic performance. Hence, it is important to find the optimum carburization temperature balance between a high purity grade of Mo_xC_y and excessive carbon deposition. The optimization of the carburization conditions was conducted by primarily studying the catalysts Mo_2C/SBA-15-HNC and Mo_2C/SiO_2-WI.

The carburization of Mo_2C/SBA-15-HNC at 873 K was followed by means of *in situ* XRD and TGA analysis. According to the XRD patterns and the corresponding Rietveld analysis results (see Figure 2-A, B & C), the reduction of orthorhombic MoO_3 (PDF – 00-005-0508, SPGR Pbnm (62)) to MoO_2 (PDF – 04-003-1961, SPGR p21/c (14)) is first observed at 675 K, becoming the dominant phase at 764 K. Simultaneously, the average crystallite size reduces slightly. First signs of the carbide (as η-$MoC_{0.59}$, PDF – 04-013-5833, SPGR p63/mmc (194)) formation can be observed by a broad reflection at 853 K, followed by β-Mo_2C (PDF – 00-035-0787, SPGR p63/mmc (194)) at 873 K. After 5 minutes at 873 K the MoO_2 reflections disappear completely. TGA analysis (see Figure 2-D) shows four significant weight losses, with the first signal as a small broad signal at 523 K. This observation is in contrast with the first detection of oxide reduction at 675 K

by XRD, but it can be rationalized by an incomplete calcination process from AHM to MoO_3 prior to TGA analysis, which is also shown by the continuous loss of mass from the beginning of the experiment (around 5 wt.-% in total). This is followed by a large and prolonged drop in mass which is associated to the reduction of MoO_3 to MoO_2 starting at 680 K with maximum at 740 K. At around 840 K, the signal observed is linked to the formation of the carbide. The carburization process lasts for at least 2.5 hours, after which no further change in weight is observed. TGA results captured during the carburization of bulk MoO_3 (see Figure S2-A) unravel that there is no weight loss until 723 K. Upon the formation of the carbide in the bulk sample, the measured weight loss is briefly higher than expected for a full conversion to the carbide. This could be explained by a partial reduction of MoO_2 to a metallic form prior to the incorporation of carbon in the structure. In the supported sample this behavior could not be resolved possibly due to the lower Mo concentration in the sample. However, the carbide formation for the supported sample appears to be more facile at 873 K, whereas the bulk sample only fully carburized at 923 K.

During the carburization process of Mo_2C/SiO_2-WI, *in situ* XRD (see Figure 2-E, F & G) evidences the decomposition of ammonium decamolybdate ($(NH_4)_8Mo_{10}O_{34}$, PDF – 00-037-0381, SPGR P-1 (2)) to ammonium tetramolybdate ($(NH_4)_2Mo_4O_{13}$, PDF – 04-011-4665, SPGR P-1 (2)), which is first detected at 454 K. The average crystallite size increases slightly during the transition of these two phases from around 5 nm to 10 nm. The molybdate precursor is fully decomposed by 500 K, where a mixture of hexagonal (PDF – 00-065-0141, SPGR p63/m (176)) and orthorhombic MoO_3 is formed with a crystallite size of around 9 and 6 nm, respectively. The orthorhombic phase becomes the dominant phase at 620 K with a slight increase in crystallite size to around 9 nm. The reduction of MoO_3 to MoO_2 proceeds slowly, reflected by a long phase overlap, with the first MoO_2 diffractions appearing at 636 K to eventually become a pure MoO_2 phase at 739 K with a crystallite size of around 12 nm. The molybdenum carbide, in form of β-Mo_2C and η-Mo_2C, is initially observed after holding at 873 K for 25 minutes and is the dominant phase after 95 minutes at 873 K. The final carbide phase consists of a mixture of β-Mo_2C (44 wt.-%) and η-Mo_2C (56 wt.-%) with crystallite sizes of around 4 and 3.8 nm, respectively. The TG and DTA curves (see Figure 2-H) are again very much in line with

the XRD results, showing four significant weight changes and one small and broader signal, while increasing temperature. Together with the XRD analysis it can be confirmed that the two losses at approximately 442 and 520 K represent the decomposition of the molybdate to MoO_3. The small broad signal indicates the transition from hexagonal to orthorhombic MoO_3. At 723 K, a major weight loss is associated to the reduction towards MoO_2. Finally, at 873 K the carburization of MoO_2 to Mo_2C takes place, which is completed after an hour time on stream. Similar observations are made during the carburization of bulk AHM (see Figure S2-B) and in the study by Wienold et al.[29] reporting on the decomposition of AHM in a diluted H_2 atmosphere at elevated temperatures.

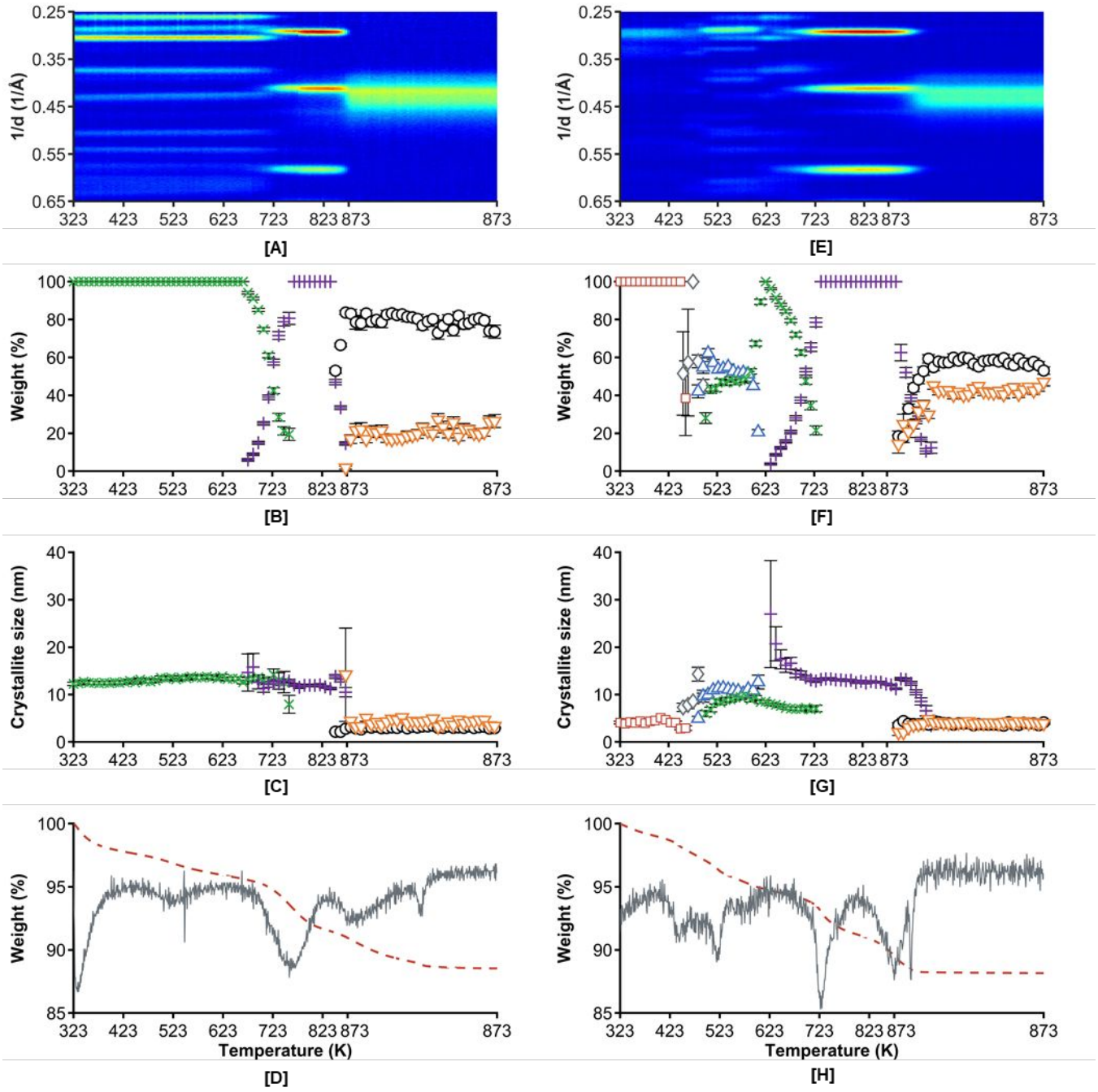

Figure 2. Carburization procedure of Mo_2C/SBA-15-HNC (A-D) and Mo_2C/SiO_2-WI (E-H) displayed by the top view of *in situ* XRD patterns **[A & E]**, the corresponding Rietveld analysis with phase composition and particles size of the different Mo phases **[B, C, F &**

G] (□ $(NH_4)_8Mo_{10}O_{34}$; ◇ $(NH_4)_2Mo_4O_{13}$; △ MoO_3 (hexagonal), × = MoO_3 (orthorhombic), + = MoO_2, ○ = η-$MoC_{0.59}$, ▽ = β-Mo_2C) and TGA analysis **[D & H]** with TG curve (dashed line) and DTA signal (solid line). Conditions: T = 873 K; P = 1 atm; ramp rate of 1 K/min; holding time 5 hours; for detailed information on gas composition and space velocities, see experimental section.

The carburization of Mo_2C/SiO_2-WI was also studied by *in situ* Raman spectroscopy (see Figure S3). The molybdate precursor is fully decomposed below 473 K under both air and carburization atmosphere. However, the decomposition pathway seems to be influenced from the early stages under different atmospheres, as is indicated by the Raman band at 963 cm^{-1}. Interestingly, at temperatures above 473 K, under carburization conditions, no clear Raman spectra for MoO_3 or MoO_2 are observed. A small broad band is observed at 523 and 573 K around 721 cm^{-1} which can be linked to the MoO_2 species, but it disappears at 623 K.[28] Since Raman is not a bulk technique relying on long range order, these observations may suggest that the surface of the Mo particles carburize at much lower temperatures than for the bulk of the crystallites, as is observed by XRD. On

the contrary, calcination of the precursor in air atmosphere under otherwise identical experimental settings led to the detection of prominent MoO_3 Raman bands at 665 cm^{-1} ($\nu(OMo_3)$), 817 cm^{-1} ($\nu(OMo_2)$) and 994 cm^{-1} ($\nu(Mo{=}O)$) in the entire temperature range of 423-873 K. In our previous study, bulk carburized samples show MoO_3 Raman spectra after passivation, even though invisible to laboratory XRD analysis.[18] The observed MoO_3 was proposed to be in form of an amorphous passivation layer formed before removal from the reactor. However, our latest *in situ* Raman spectroscopy results (see Figure 3) show that after the carburization of the catalyst, followed by passivation at room temperature, no MoO_3 is formed. This can be explained by a report of Ovari et al.[30], who observed that at room temperature O_2 dissociates on the carbide surface but does not oxidize it. The passivated sample was then exposed to a reactivation treatment in an attempt to remove/re-carburize the oxygen/oxide surface layer (heated up to 873 K at 3 K/min under 10 vol.% CH_4, 40 vol.% H_2, balance He, and held at 873 K for 1 hour) and again spectra were collected at RT and no Raman bands were observed. No signal associated to carbon deposits was detected either. Subsequently, the reactivated sample was passivated as described above, exposed to an air atmosphere overnight at RT and

again spectra were collected, first in an inert atmosphere followed by an air atmosphere. In an inert atmosphere, neither MoO_3 nor MoO_2 were observed. The measurement in air atmosphere clearly showed oxidation, confirming that a local energy input due to laser irradiation in the presence of oxygen is necessary for the oxygen to react with the surface carbon resulting in the oxidation of the carbide to MoO_3 (Raman bands at 817 and 991 cm^{-1}).

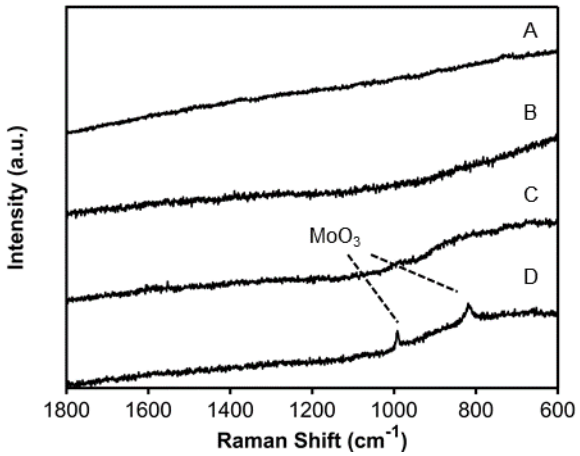

Figure 3. *In situ* Raman spectra for Mo_2C/SiO_2-WI collected: **[A]** at RT after passivation treatment, **[B]** at RT after reactivation treatment of passivated catalyst, **[C and D]** at RT after exposure of the passivated-reactivated-passivated catalyst to air at RT overnight. Spectra A, B and C are collected under He atmosphere, spectra D under air atmosphere.

Ex situ XAS analysis was performed on bulk β-Mo_2C samples, carburized at different temperatures. In addition, the samples were exposed to air with and without a prior passivation treatment to study phase stability under atmospheric conditions. The XANES spectra as well as the XRD patterns can be found in the supplementary information (Figure S4 and S6). To quantify the changes in the XANES region (indicated by the red arrows in Figure S4), each spectrum was fitted by means of a linear combination of MoO_3, MoO_2 and β-Mo_2C (see

Table **1** and Figure S5). Note that by means of XRD analysis, the bulk carbides did not show any traces of η-$MoC_{0.59}$ nor MoO_xC_y (see Figure S6 and Table 1), although this does not necessarily exclude them to be present on the surface. At a carburization temperature of 873 K, the efficiency of a passivation treatment is evidenced by the significant difference in MoO_2 content (26.7 ± 0.7 wt.-% with passivation and 32.1 ± 0.8 wt.-% without passivation) suggesting a re-oxidation. XRD analysis of the non-passivated sample carburized at 873 K indicates the presence of 5 wt.-% MoO_2 in the form of large crystallites (105.3 ± 9.8 nm). This is potentially originating from sintering due to the strong exothermic re-oxidation reaction, leading to localized temperature spikes, when suddenly exposed to a high concentration of oxygen (see Figure 4-A), such as in air. It appears that O_2 dissociation on the carbide surface without causing an oxidation of the Mo phase only proceeds when the oxidant is introduced at low concentrations at room temperature[30] or lower, hence the passivation treatment of 1 vol.-% O_2, preventing bulk oxidation (see Figure 4-B). With increasing temperature of carburization, the content of MoO_2 in the samples decreases, independent of a previous treatment and the crystallite size of the carbide phase increases. While the latter is probably the effect of enhanced sintering

during carburization, the former can be associated to the previously reported increase in carbon deposits creating a protective layer around a carbide core (see Figure 4-C). The MoO_2 content is believed to be a residue from the synthesis rather than stem from the re-oxidation by air, possibly in form of a core with a thick carbide shell too small/thin for XRD to detect.

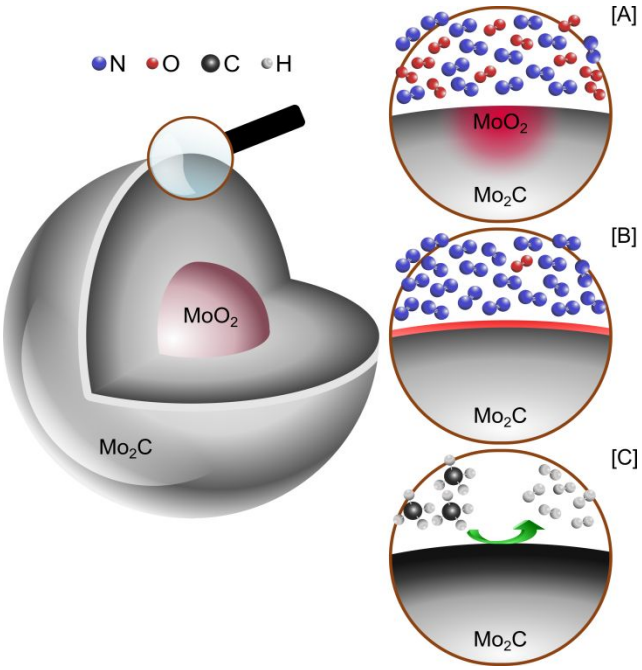

Figure 4. Schematic representation of a bulk Mo_2C particle with residual oxide core and different possible surface states and their effect on reactivity: **[A]** A bare carbide surface is partially re-oxidized causing (and subsequently accelerated by) localized temperature spikes when exposed to high concentrations of oxygen such as in air. **[B]** O_2 is dissociated

on a bare carbide surface at low partial pressures of the oxidant forming a passivating layer around the carbide particle. **[C]** A thick layer of carbon deposits around the carbide particle at higher carburization temperatures protecting the carbide surface from re-oxidation in air (compare case [A]).

Table 1. Phase composition via XANES and XRD Rietveld analysis on bulk β-Mo_2C carburized at different temperatures and exposed to air with (P) or without (NP) a passivation treatment.

Sample	XANES		XRD			
	MoO_2 (wt.-%)	β-Mo_2C (wt.-%)	MoO_2 (wt.-%)	Crystallite size (nm)	β-Mo_2C (wt.-%)	Crystallite size (nm)
873 K-P	26.7 ± 0.7	73.3 ± 1.0	n/a	n/a	100.0	7.5 ± 0.1
873 K-NP	32.1 ± 0.8	67.9 ± 1.0	5.7 ± 0.2	105.3 ± 9.8	94.3 ± 0.2	7.3 ± 0.1
923 K-P	24.7 ± 0.8	75.3 ± 1.1	n/a	n/a	100.0	9.0 ± 0.1
923 K-NP	24.3 ± 0.8	75.7 ± 1.1	n/a	n/a	100.0	8.7 ± 0.1
973 K-P	16.9 ± 0.5	83.1 ± 0.8	n/a	n/a	100.0	13.8 ± 0.6
973 K-NP	18.7 ± 0.6	81.3 ± 0.9	n/a	n/a	100.0	14.3 ± 0.7
1023 K-P	5.8 ± 0.7	94.2 ± 1.0	n/a	n/a	100.0	13.1 ± 0.6
1023 K-NP	5.9 ± 0.6	94.1 ± 0.9	n/a	n/a	100.0	14.9 ± 0.8

Characterization of activated catalysts. Based on the results obtained studying the carburization process, all samples evaluated for RWGS activity, including Mo_2C/SiO_2-SG and Mo_2C/SBA-15-WI, were carburized at 873 K for 5 hours with a ramp rate of 1 K/min.

XRD analysis confirmed the presence of a carbide phase. The compositions of the carbides are determined via Rietveld refinement (Figure S7) and are listed in Table 2.

Interestingly, the refinements of Mo_2C/SBA-15-HNC and Mo_2C/SiO_2-SG suggest the presence of a different phase than β-Mo_2C, as was observed by *in situ* XRD (see Figure 2). The reflections at 1/d-spacings 0.41 and 0.48 can either be related to a cubic MoO_xC_y phase (PDF 00-017-0104) or α-$MoC_{0.68}$ (PDF 01-082-3210, SPGR Fm-3m (225)).[31,32] The latter phase is usually synthesized by a carburization procedure of Mo_2N[11] or when promoted with platinum[33], we therefore suggest that the observed phase is more likely to be MoO_xC_y, indicating the presence of an intermediate phase between the reduction and carburization step.[34] β-Mo_2C is observed when the same samples are carburized at slightly higher temperatures (see Figure S8), supporting this assumption. These discrepancies between *in situ* XRD and reactor carburization could be associated to variations in heating system and gas flow patterns resulting from the differences between the dedicated fixed bed reactor and the XRK 900 reactor chamber and reaffirm the sensitivity of the physical properties of Mo_xC_y on the carburization process, specifically at smaller particle sizes. In this work, the molybdenum oxycarbide was described as cubic

structure (space group: Fm-3m) with a stoichiometry of MoOC, as the MoO_xC_y phase (PDF 00-017-0104) is insufficiently described in literature and no pure phase was available prohibiting the use of alternative Rietveld Refinement strategies such as PONKCS.[35]

Table 2. Overview of phase quantification and crystallite sizes determined via Rietveld analysis of freshly carburized catalysts at 873 K.

Sample	Phase composition (wt.-%) / crystallite size (nm)					
	β-Mo_2C		η-$MoC_{0.59}$		MoO_xC_y	
	wt.-%	nm	wt.-%	nm	wt.-%	nm
Mo_2C/SBA-15-HNC	-	-	45.5 ± 4.6	3.4 ± 0.5	54.5 ± 4.6	4.0 ± 0.4
Mo_2C/SiO_2-WI	21.4 ± 2.7	4.9 ± 0.8	78.6 ± 2.7	3.3 ± 0.2	-	-
Mo_2C/SiO_2-SG	-	-	55.8 ± 4.3	4.4 ± 0.5	44.2 ± 4.3	5.7 ± 0.8
Mo_2C/SBA-15-WI	19.4 ± 2.9	9.2 ± 2.0	80.6 ± 2.9	4.6 ± 0.4	-	-

By means of TEM analysis it was confirmed that the carbide particles are evenly distributed over the SiO_2 support and no large variations in terms of particle size are observed. Due to the low contrast between the small carbide particles and the support, a

reliable particle size distribution could not be extracted (see Figure 5) but the sizes measured are in line with the data obtained from XRD. No signs of carbon formation are observed. Raman spectroscopy was employed to further probe the presence of carbonaceous deposits analyzing multiple particles of each sample (see Figure S9). Mo_2C/SiO_2-WI is the only sample which showed some degree of carbon deposits identified by the D-band at 1350 cm^{-1} and the G-band at 1580 cm^{-1}. These deposits are however not found throughout the sample.

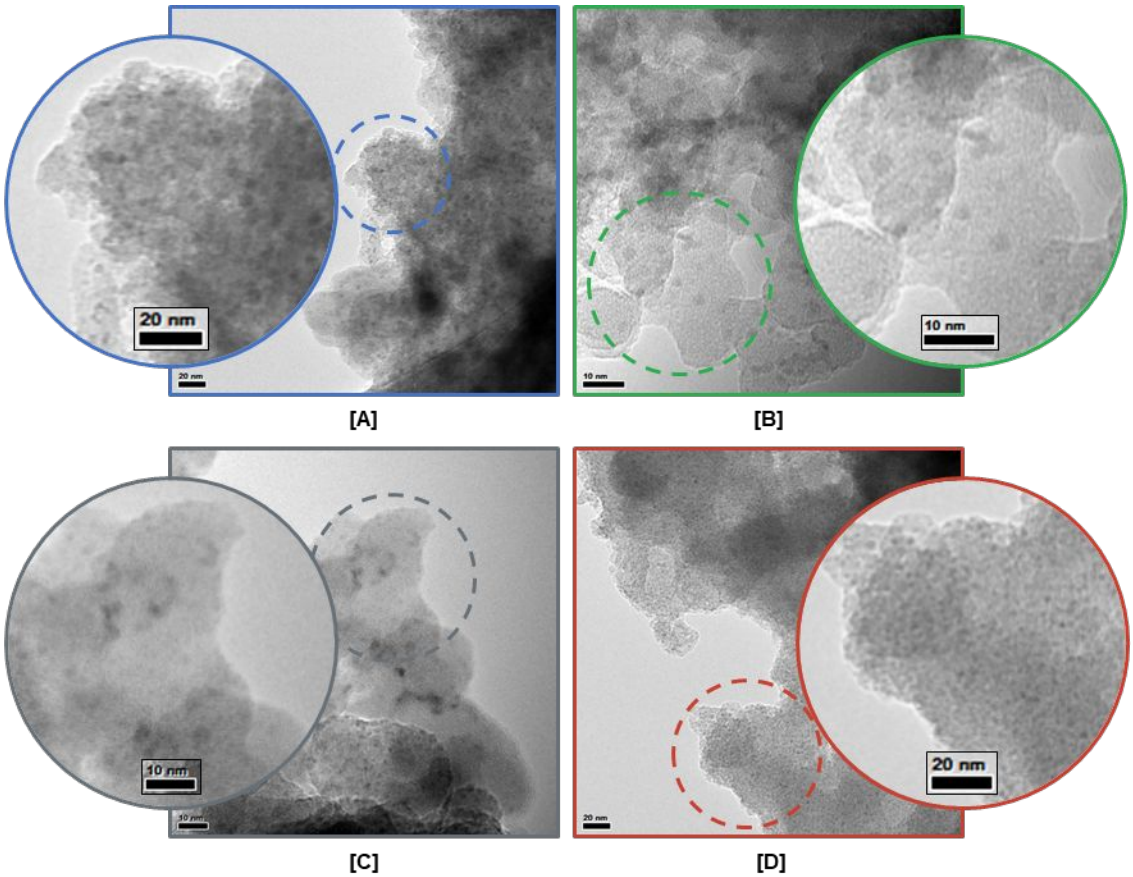

Figure 5. TEM images of [A] Mo_2C/SBA-15-HNC, [B] Mo_2C/SiO_2-WI, [C] Mo_2C/SiO_2-SG and [D] Mo_2C/SBA-15-WI.

Probing CO_2 activation on Mo_2C by temperature programmed reaction of CO_2. The activation of thermodynamically stable CO_2 is the key step in the RWGS reaction. The formation of CO as function of temperature was used as probing reaction in the present study both using a fixed-bed reactor set-up and *in situ* XAS. In the reactor studies, CO formation is first observed in the temperature range between 500 K and 600 K

independent of synthesis route (see Figure 6-A). At higher temperatures, between 800 K and 850 K, the CO formation rate increases significantly, reaching a maximum concentration of CO in the reactor outlet gas between 880 K and 920 K. When normalizing the CO formation rate to Mo content (see Figure 6-A & B), Mo_2C/SiO_2-SG and Mo_2C/SiO_2-WI show the highest yield of CO with Mo_2C/SiO_2-SG reaching the peak formation rate at significantly lower temperatures (892 K vs. 917 K) suggesting a higher intrinsic activity or rather a higher affinity for re-oxidation. No correlation can be observed between the average mass specific Mo surface area of all four freshly carburized samples (Table S5) and the observed CO formation rates and yield. After the reaction, all four supported samples are oxidized to MoO_2 with an increased average crystallite sizes between 21 and 29 nm, leading to a significant decrease in the average mass specific Mo surface area.

Two main pathways can lead to the formation of CO. Option 1: CO_2 dissociates on the catalyst surface to CO and surface oxygen species, leading to the possible formation of molybdenum oxycarbide (MoO_xC_y) on the surface and eventually bulk oxide. Option 2: via the reverse Boudouard reaction, removing carbon either from earlier deposited

surface carbon or from the carbide. To understand which pathway is preferred, a similar CO_2 activation experiment is performed on bulk β-Mo_2C as higher quantities of CO are formed thus limiting uncertainties in data acquisition (see Figure 6-C). Surface activation of CO_2 will lead to an equal amount of CO formed compared to CO_2 reacted while the removal of carbon yields two moles of CO per mole of CO_2 reacted. Since there were no other products observed, it is possible to assign all CO_2 reacted to CO formed. At temperatures below 800 K, the molar rate of CO formed, and CO_2 reacted is equal, which suggests the CO_2 surface activation pathway to be dominant. At higher temperatures, the molar rate of CO formed is larger than CO_2 reacted, but the ratio is lower than 2. This could suggest that initially, due to CO_2 dissociation on the surface, oxygen species on the carbide surface are formed potentially leading to an oxycarbide like structure and subsequently, at temperatures above 800 K, the surface oxygen species react with the carbon species from the carbide structure, liberating CO and forming MoO_2 (Figure S10). The observed drop in CO formation at around 950 K and the remaining carbide in the bulk sample, suggest that CO_2 dissociation is happening on the top surface layer(s) only and once these layers are oxidized, the catalyst becomes inactive for CO_2 activation. The

incomplete oxidation of the bulk sample is likely due to the larger crystallite size resulting in a dense oxide layer protecting an inner carbide core.

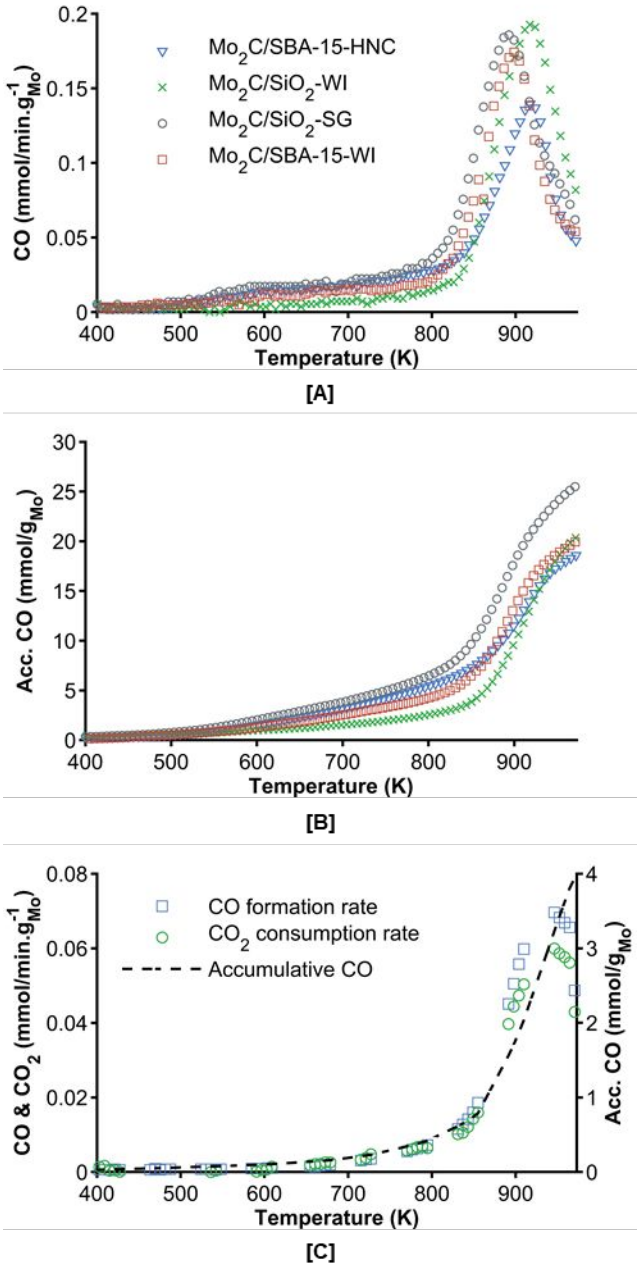

Figure 6. **[A]** CO formation rate and **[B]** accumulative formation of CO as a function of temperature normalized to Mo mass in the catalyst. **[C]** CO_2 activation over bulk β-Mo_2C

as function of temperature. Conditions: ramp from 323 K to 973 K at 1 K/min in 1 vol.-% CO_2 in N_2 (SV = 60 L/h·g_{cat}^{-1}) at 1 atm.

In situ XAS experiments were performed on three out of the four supported samples; Mo_2C/SiO_2-WI (Figure 8), Mo_2C/SBA-15-HNC (Figure S11) and Mo_2C/SiO_2-SG (Figure S12). Each sample was exposed to an *in situ* carburization treatment followed by a temperature programmed reaction in 1 % CO_2/He. It must be highlighted that the carburization and CO_2 temperature programmed activation conditions vary from the earlier described synthesis and reactor studies. Under carburization conditions, the temperature was ramped to 650 K (10 K/min), followed by a further ramp to 920 K (2 K/min) holding at 920 K of 2.5 hours. During exposure to CO_2, the temperature was ramped to 600 K (10 K/min) followed by a ramp to 1010 K (5 K/min) holding at 1010 K for 1 hour. XAS measurements were taken at room temperature before (referred to as RT-1) and after the two different treatments (RT-2 and RT-3, respectively) and XANES measurements were recorded throughout the temperature ramping. The *in situ* XANES spectra of Mo_2C/SiO_2-WI are presented by a top view plot (see Figure 8-A & B)

accompanied by the linear combination fitting results of the different Mo-phases (see Figure 8-C & D). Unlike the *in situ* XRD results (Figure 2), but similar to the *in situ* Raman observations (Figure S3), no clear MoO_3 spectra is observed during the decomposition of the molybdate precursor in the presence of the carburization gas mixture (see Figure 7). This can be explained by the differences in temperature ramp rate between XRD (1 K/min), Raman (3 K/min) and XAS (10 K/min) and sample presentation. Note that small differences in signal intensity in the spectra, between RT-1 and MoO_2 can be observed (indicated by the arrow in Figure 8-A). Due to the unavailability of further reference materials, RT-1 was used as reference for the molybdate in the XANES LCF.

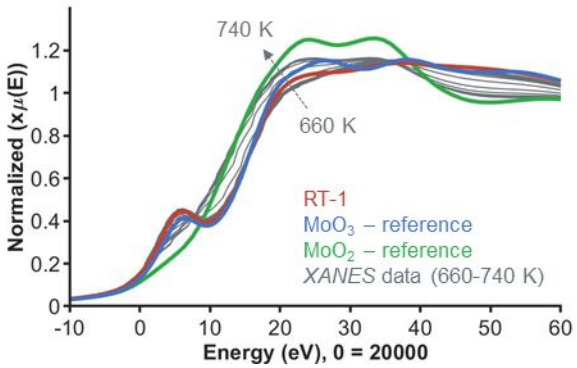

Figure 7. Normalized *in situ* XANES spectra (around Mo K-edge) of Mo_2C/SiO_2-WI during carburization from 660 K to 740 K, energy scale shifted to 20,000 eV.

At 720 K a phase change from the molybdate to MoO_2 is observed (see Figure 8-A). Linear combination fitting results suggest that the carburization of the formed oxide phase starts almost simultaneously, indicating a much lower carburization onset temperature than observed by XRD, but supporting the earlier described *in situ* Raman observations. The maximum MoO_2 content in the sample was observed to be ±50 wt.-%. At 790 K the carbide phase becomes the dominant phase, reaching ±95 wt.-% carbide content at 825 K. No significant changes in the Mo-phase composition are observed during the 2.5 hour isothermal conditions at 920 K.

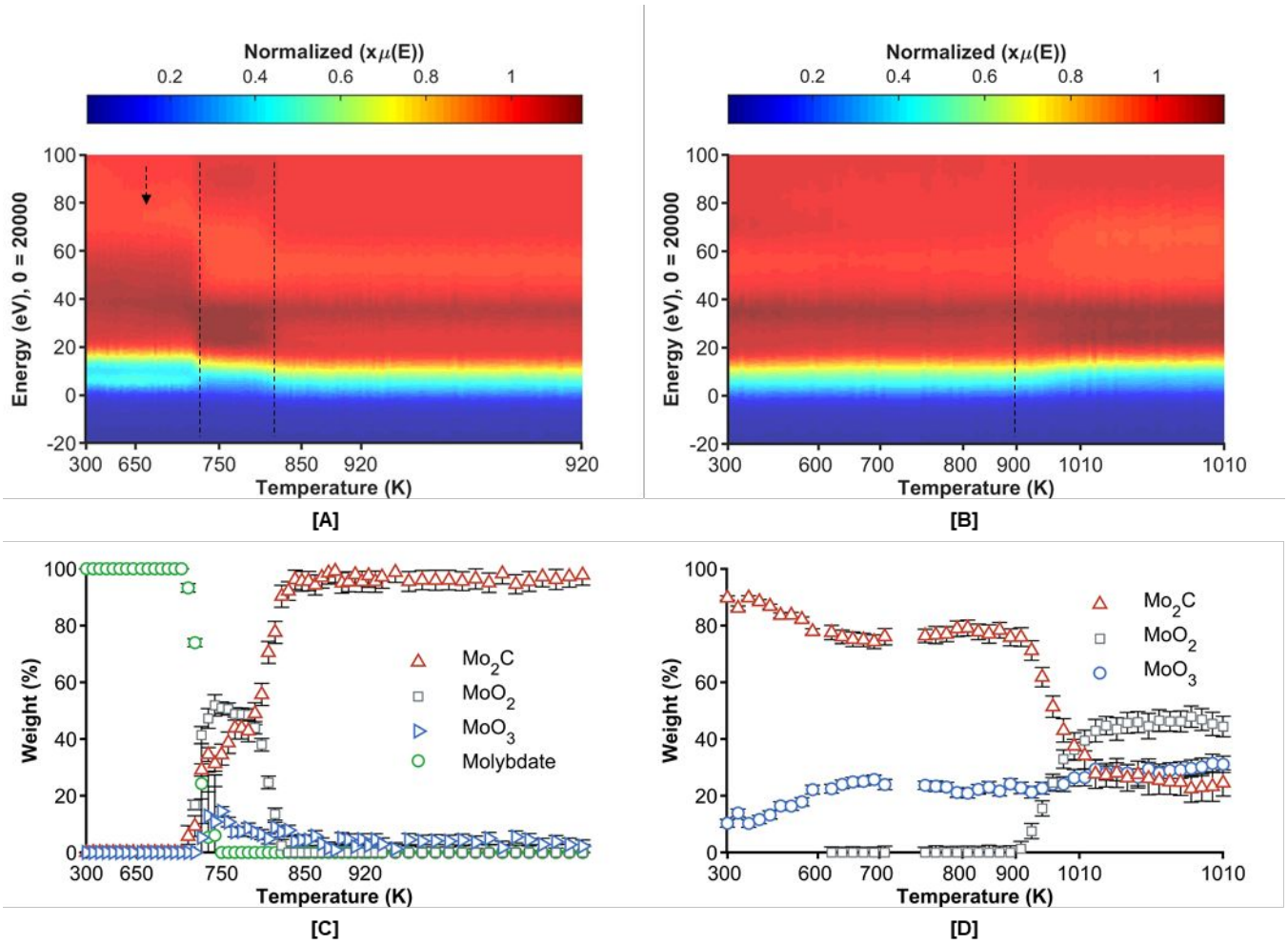

Figure 8. In situ XANES spectra on Mo_2C/SiO_2-WI, with **[A]** carburization treatment, and **[B]** CO_2 activation and their corresponding LCF results **[C]** and **[D]**, respectively; analogous in situ XANES spectra are given in the ESI for Mo_2C/SBA-15-HNC (Figure S11) and Mo_2C/SiO_2-SG (Figure S12). For detailed conditions see experimental section.

The *in situ* XANES carburization of Mo_2C/SBA-15-HNC displays two significant phase changes from MoO_3 to MoO_2 to Mo_2C (see Figure S11). The reduction of MoO_3 to MoO_2

starts at 735 K. The formation of the carbide again appears to start simultaneously. The maximum MoO_2 content reached is ±42 wt.-% at 775 K, with the carbide becoming the dominant phase at 785 K. The final carbide content of ±88 wt.-% is observed after about 30 minutes holding at 920 K, with the remainder being mainly MoO_3. Mo_2C/SiO_2-SG, also starting from the MoO_3 phase, shows similar behavior during carburization (see Figure S12) with the reduction of MoO_3 starting at 685 K and simultaneously forming the carbide phase. The maximum MoO_2 content was observed at 745 K (±51 wt.-%) with the carbide phase becoming dominant at 770 K. The final carbide composition is estimated at ±94 wt.-%, mainly balanced by MoO_3. The observed differences in onset temperatures between the three samples (SG < WI < HNC) are clearly evidencing a dependency of synthesis route and/or type of support material, during the early stages of the carburization process.

The compositions obtained from LCF of the XANES spectra collected at room temperature, after the carburization treatment, are in line with the above observations (see Table S2 and Figure S13). The slight discrepancy between the fitting results of the RT spectra and *in situ* spectra can be rationalized by the noise induced at high

temperatures but are within the usual LCF error (±10 wt.-%). These compositions cannot be directly compared to the samples prepared inside the reactor, due to different carburization protocols with the higher ramp rate to be most likely the main cause for the leftover oxidic species.

EXAFS analysis was performed to further investigate the different Mo allotropes present in the samples as the normalized XANES spectra do not indicate clear differences between β-Mo_2C and α-$MoC_{0.68}$ (no reference materials available for η-$MoC_{0.59}$ and MoO_xC_y). In k-space, small but clearly visible features can be identified, distinguishing between the two carbide phases (indicated by arrows in Figure 9-A). These observations confirm that no alpha-carbide phase is present. In R-space, the first and second shell, Mo-C and Mo-Mo, are indistinguishable between the alpha and beta carbide phase and each sample can be fitted with a crystal structure corresponding to the beta-carbide phase. The only difference observed is between 4.5 and 6.0 Å (see Figure 9-B). All fits and corresponding fit parameters can be found in Figure S13 and Table S3.

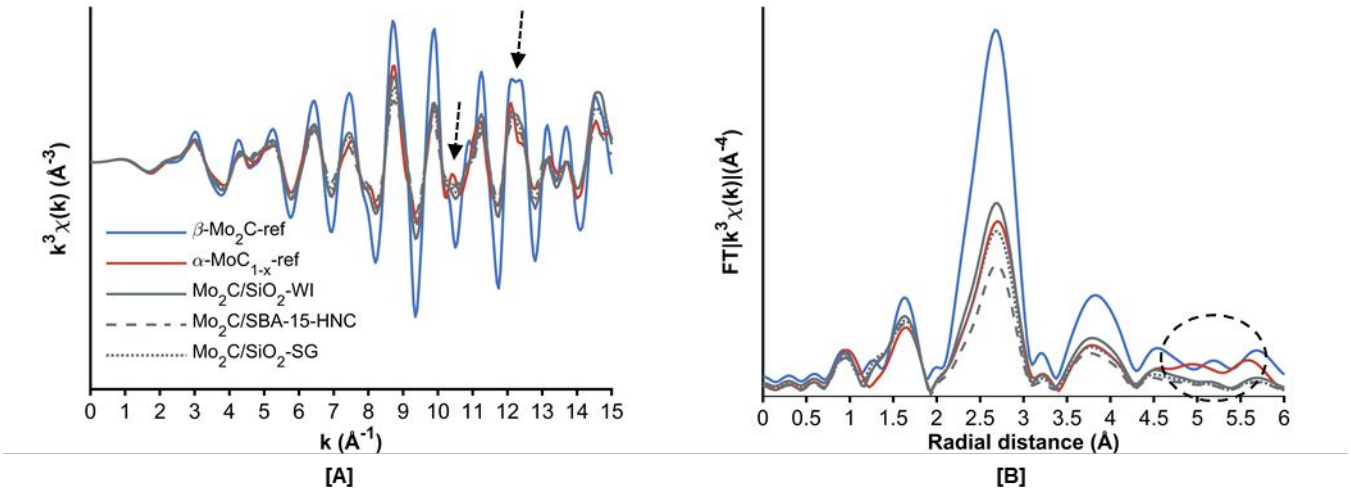

Figure 9. k^3- weighted Mo K-edge EXAFS spectra of Mo_2C/SiO_2-WI, Mo_2C/SBA-15-HNC, Mo_2C/SiO_2-SG, β-Mo_2C-reference and α-MoC_{1-x}-reference in [A] the k-space and [B] the R-space.

During the temperature programmed reaction with CO_2 over the freshly carburized samples, one significant step change in the XANES spectra is observed for all samples (see Figure 8-B, Figure S11-B and Figure S12-B). LCFs of the *in situ* XANES spectra show that the oxidation onset temperature of Mo_2C to MoO_2 (and MoO_3) is between 905 and 925 K. These results confirm the observations made during the reactor studies, despite the difference in temperature ramp rate. This strengthens the previously proposed CO_2 activation mechanism. Contrary to the XRD analysis after the reactor studies, the

LCF results of the XAS spectra after CO_2 activation (see Table S2) indicate that the carbide does not only oxidize to MoO_2, but also to MoO_3. These results show that the MoO_3 its crystallinity is insufficient to be observed by XRD, e.g. that amorphous MoO_3 is formed or it is located at the surface of the particles. A study presented by Solymosi et al.[36] confirms the possible (surface) oxidation of Mo_2C to MoO_3 in the presence of CO_2 by means of XPS analysis. MoO_3 is reported as the dominant species at reaction temperatures of 1073 K.

Reverse water-gas-shift reaction. Finally, all four samples were tested for RWGS activity in a range of reaction conditions with varying CO_2 : H_2 ratio and to probe the influence of supported carbide catalysts. At every temperature and H_2 to CO_2 feed ratio, the thermodynamic equilibrium conversion (X_{eq}) of the RWGS reaction was calculated for comparison to make sure that the observed conversion is not limited by thermodynamics. At a temperature of 673 K, a H_2 to CO_2 ratio of 1 (X_{eq} = 22.1 %) and a space velocity of 60 L/h.g$^{-1}_{cat}$ (of which 50 vol.-% is argon), the catalysts Mo_2C/SiO_2-WI and Mo_2C/SBA-15-HNC show very similar conversions, close to X_{eq}, with X_{CO_2} = 17 % and X_{H_2} = 19 %

for Mo_2C/SiO_2-WI (see Figure 10-A and Figure 10-C). Mo_2C/SBA-15-WI is less active with a CO_2 and H_2 conversion of 11 % and 12 %, respectively. Freshly carburized, the molybdenum phases of both catalysts prepared via wetness impregnation consist of approximately 80 wt.-% η-$MoC_{0.59}$ and 20 wt.-% β-Mo_2C (see Table 2). While the SBA-15 supported sample displays a slightly larger crystallite size for both carbide phases, this is somewhat overcompensated by the higher Mo content (see Table S5). During the exposure to RWGS conditions at different temperatures (see Figure 9A), the carbide phase of Mo_2C/SBA-15-WI transitions fully into a pure η-$MoC_{0.59}$ without crystallite growth, while the composition of Mo_2C/SiO_2-WI remains largely unchanged with some crystallite growth (see Tables S4 & S5). At what stage of the reaction the transition occurs is unfortunately currently unknown. The higher activity of the SiO_2 supported catalyst can be associated to the retention of the beta carbide phase which has previously been identified as more active in a study by Wan et al.[37] Mo_2C/SBA-15-HNC, only tested at 673 K for 24 hours, also transforms to a pure η-$MoC_{0.59}$, starting from a 30 wt.-% oxycarbide content (see Tables 2 & S4). The catalyst's activity is on par with Mo_2C/SiO_2-WI and outperforms Mo_2C/SBA-15-WI by 100 K (see Figure 9 A 12 to 24 hours TOS) while

displaying very comparable phase compositions and crystallite sizes (analysis of the spent catalysts, see Table S4). The overall carbide surface area appears not to be responsible for the observed difference in performance, which is mirrored in the formation rate of CO in the CO_2 activation experiments between 600 and 850 K (see Figure 6-B). A previous study by Kurlov et al. suggests that molybdenum oxycarbide is the active phase for the RWGS reaction.[38] The different synthesis routes chosen can affect other parameters such as the location of the carbide crystals on the support.

In terms of product selectivity, all catalysts show >98 % CO selectivity and <1 % CH_4 selectivity (see Figure 10-E and Figure 10-F). This clearly indicates that the CO_2 and CO methanation reactions, which are under these temperature conditions thermodynamically favored over the RWGS (see Figure 1C), are kinetically suppressed by the catalyst. The observed low concentrations of CH_4 formed can, in combination with experimental uncertainties, account for the observed temperature and sample independent 2-3 % over stoichiometric hydrogen conversion.

Increasing the H_2 to CO ratio at a reaction temperature of 673 K is, based on thermodynamic considerations, a more favorable condition for CO_2 methanation.

However, when using the RWGS to activate CO_2 together with green hydrogen to produce synthesis gas and subsequent fuels and chemicals, it is of interest to operate the RWGS at a higher than stoichiometric H_2 to CO_2 ratios to achieve higher CO_2 conversions and yield the desired synthesis gas composition at the reactor outlet.[39] Both Mo_2C/SiO_2-WI, the best performing catalyst at varying reaction temperatures, and Mo_2C/SiO_2-SG, the catalyst with the apparent most facile CO_2 activation, were studied at feed ratios of 1, 3.5 and 7 and an increased space velocity of 120 $L/h.g^{-1}_{cat}$ in a single experiment with intermittent flushing to set the new feed composition. At all conditions, both catalysts show similar activity and selectivity. With a feed ratio of 1, X_{CO_2} is between 11 and 12 %, with minimum deactivation over 24h time on stream and X_{H_2} of 15 to 16 %, which decreases to 12 to 13 % after 24h time on stream. Increasing the feed ratio to 3.5 (X_{eq} = 39.0 %) the CO_2 conversion increases to 21 % for both catalysts, with again minimum deactivation observed after 24h time on stream. A hydrogen conversion of 6 % corresponds to a 1:1 conversion ratio in moles. A feed ratio of 7 (X_{eq} = 50.7 %) further increases conversion levels without changing the stability of the catalyst. At the highest feed ratio, a methane

selectivity of approximately 2 % is recorded, which decreases steadily with time on stream to below 1 %. While in the freshly carburized samples, Mo_2C/SiO_2-WI and Mo_2C/SiO_2-SG show clear differences, namely 20-24 wt.-% of the carbide phase in form of β-Mo_2C or oxycarbide for Mo_2C/SiO_2-WI and Mo_2C/SiO_2-SG respectively, the composition of the spent catalysts is nearly identical. Compared to the RWGS experiment at different temperatures, the β-Mo_2C component is hardly retained resulting in a mostly η-$MoC_{0.59}$ active phase with very similar crystallite sizes. For a closer comparison of the catalytic performance, the accumulated CO formed per feed ratio is calculated as function of time on stream (see Figure 10). It is apparent that at a feed ratio of H_2:CO_2 of 1, the catalyst prepared via the sol gel technique shows slight advantages compared to Mo_2C/SiO_2-WI, but at a feed ratio of 3.5 this trend is reversed. No difference in performance is observed at the highest hydrogen concentration (H_2:CO_2 of 7). As discussed earlier, Mo_2C/SiO_2-SG also shows the high propensity to activate pure CO_2 which could be an indication of an enhanced redox activity. Such an enhancement is expected to be most prominent in the RWGS at low H_2 partial pressures.

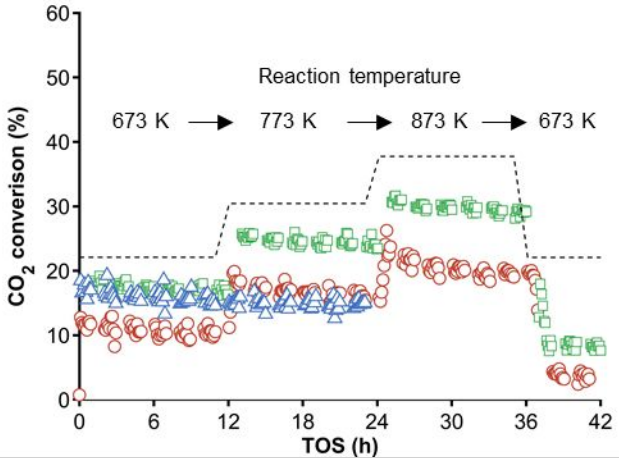
Reaction temperature
673 K → 773 K → 873 K → 673 K
CO2 conversion (%)
TOS (h)

[A]

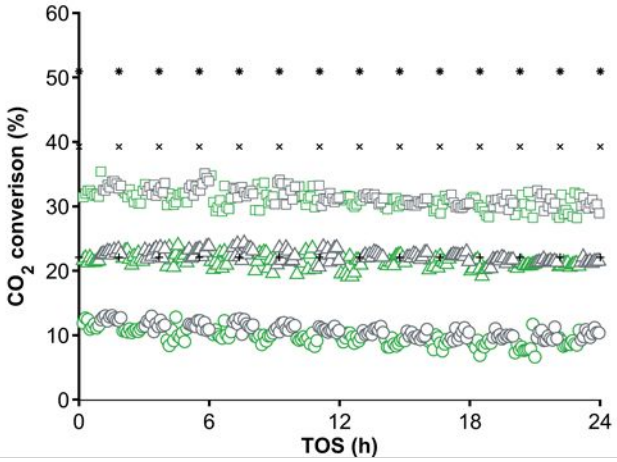
CO2 conversion (%)
TOS (h)

[B]

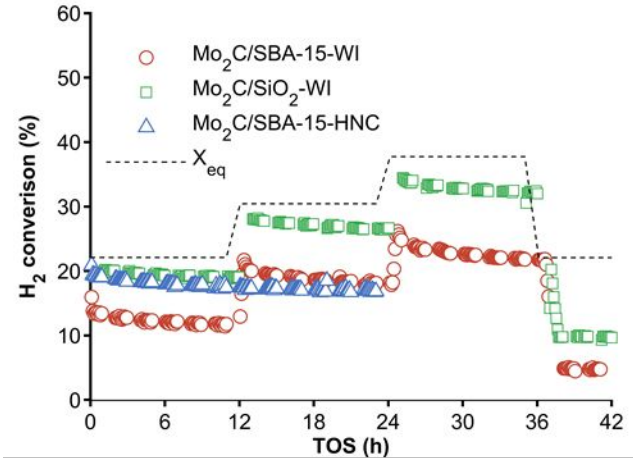
Mo2C/SBA-15-WI
Mo2C/SiO2-WI
Mo2C/SBA-15-HNC
Xeq
H2 conversion (%)
TOS (h)

[C]

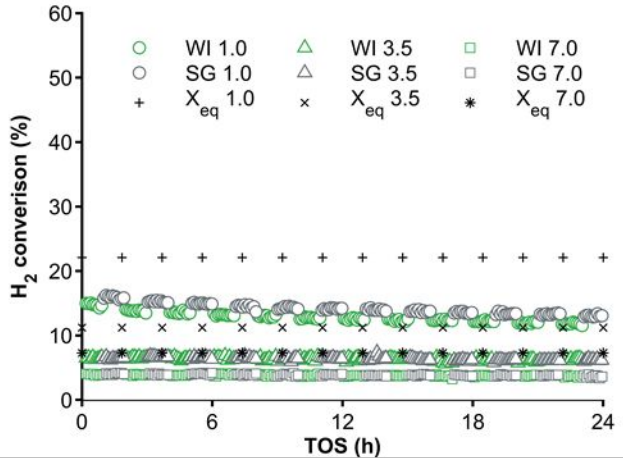
WI 1.0
WI 3.5
WI 7.0
SG 1.0
SG 3.5
SG 7.0
Xeq 1.0
Xeq 3.5
Xeq 7.0
H2 conversion (%)
TOS (h)

[D]

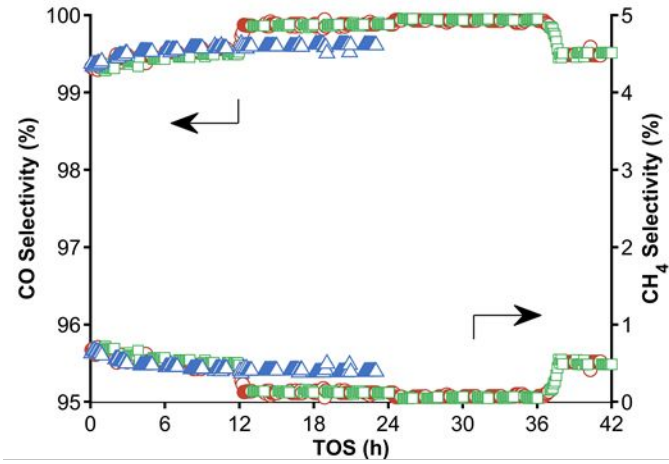
CO Selectivity (%)
CH4 Selectivity (%)
TOS (h)

[E]

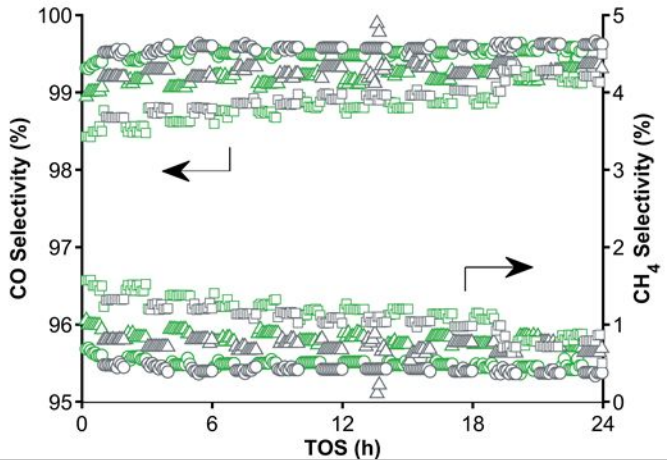
CO Selectivity (%)
CH4 Selectivity (%)
TOS (h)

[F]

Figure 10. Activity and selectivity of all catalysts under various process conditions: **[A, C and E]** □ & ○ : T = 673 K (0-12h TOS), 773 K (12-24h TOS), 873 K (24-36h TOS) and 673 K (36-42h TOS). △ : T = 673 K for 24h TOS. □, ○ & △ : H_2 to CO_2 ratio = 1, SV (CO_2+H_2) = 60 L/h·g^{-1}. **[B, D and F]** Mo_2C/SiO_2-WI (green) and Mo_2C/SiO_2-SG (grey): T = 673 K for 24h at H_2:CO_2 ratio of 1.0 (○), 3.5 (△) or 7.0 (□). SV = 120 L/h·g^{-1}. Thermodynamic equilibrium conversion for CO_2 and H_2 displayed by plusses (1.0), crosses (3.5) and stars (7.0).

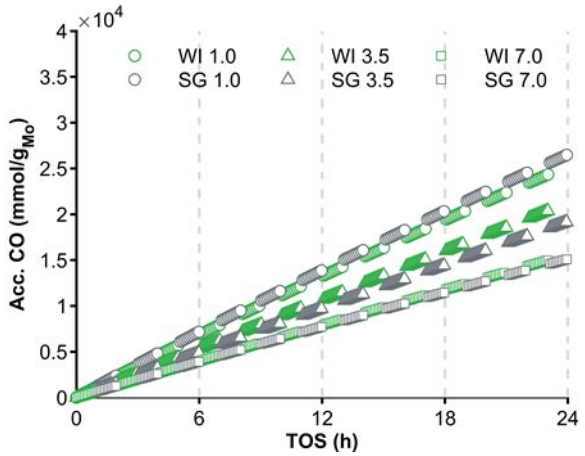

Figure 11. Accumulative formation of CO as a function of time under RWGS conditions normalized per Mo content. Mo_2C/SiO_2-WI (green) and Mo_2C/SiO_2-SG (grey): T = 673 K for 24h at H_2:CO_2 ratio of 1.0 (○), 3.5 (△) or 7.0 (□). SV = 120 L/h·g^{-1}.

CONCLUSIONS

Four different Mo_xC_y-based catalysts were successfully synthesized using three different techniques, WI, HNC and SG, on two different support materials, SiO_2 and SBA-15. The difference in synthesis methods yielded a variation in Mo_xC_y crystal phase composition (β, η or oxycarbide phase) in a similar crystallite size range. The materials carburized from MoO_3 (Mo_2C/SiO_2-SG and Mo_2C/SBA-15-HNC) seem to carburize slightly later and still contain the oxycarbide phase after treatment at 873 K. The temperature was shown to be a major parameter in the carburization procedure, not only in terms of carbon deposition, but also in carbide purity, re-oxidation sensitivity and crystallite size. The comparison of *in situ* techniques focusing both on the long- and short-range order of materials provides evidence for a surface carburization at temperatures significantly lower than reported for bulk carburization. The same techniques also suggest, in line with literature[30], that at room temperature low concentrations of O_2 (such as 1 vol.%) adsorb dissociatively on the carbide surface without causing Mo oxidation. Increasing the O_2 concentration results in violent oxidation of pristine carbide surfaces.

In a diluted CO_2 atmosphere, at temperatures up to 800 K, CO_2 is activated on the surface via dissociation. At higher temperatures the carbide is oxidized to MoO_x. Of all tested samples, Mo_2C/SiO_2-SG displays the peak CO formation rate, i.e. peak re-oxidation of the carbide phase through CO_2, at the lowest temperatures. No correlation of this observation to physical properties was found.

Under RWGS conditions, all catalysts tested show high CO_2 conversion (up to 30 %) with an outstanding CO selectivity of above 99 %, even at high H_2 to CO_2 ratios. This clearly shows the kinetic suppression of the thermodynamically favored CO and CO_2 methanation. H_2 readily removes formed oxygen surface species forming H_2O, preventing the oxidation of the catalyst. Comparing the wetness impregnation catalysts, with comparable carbide phase composition and estimated carbide surface area after the carburization, the SiO_2 supported sample outperforms the SBA-15 supported sample at all tested temperatures. During the reaction, the beta carbide contribution converts completely to η-$MoC_{0.59}$ over the SBA-15 sample, with no such phase change observed on the SiO_2 supported catalyst. When the MoO_3 hybrid nanocrystals are deposited on SBA-15, they perform on par with Mo_2C/SiO_2-WI although the initial mixture of oxycarbide

and eta carbide converts to 100 % η-$MoC_{0.59}$ after only 24 hours TOS at the lowest reaction temperature. While the exact role of the carbide phase cannot be deconvoluted from the presented data, the HNC preparation seems advantageous compared to the WI-route. The SG and the WI catalyst on SiO_2 showed very similar behavior, although Mo_2C/SiO_2-SG is shown to oxidize at much lower temperatures in a diluted CO_2 stream suggesting different redox behavior. Only at the stoichiometric feed ratio Mo_2C/SiO_2-SG seems to be slightly more active. Maybe the effect of a material specific higher redox activity is suppressed at higher hydrogen partial pressures.

In all samples, catalyst deactivation could not be prevented completely, and it is suggested to be due to a phase change from β-Mo_2C & MoO_xC_y to η-$MoC_{0.59}$ and particle sintering.

ASSOCIATED CONTENT

Supporting Information. Thermodynamic predictions for the methanation of CO_2 (Figure S1); TGA analysis of bulk MoO_3 and bulk AHM (Figure S2); ICP-OES and BET analysis results (Table S1); *In situ* Raman spectroscopic results for the calcination and carburization of AHM supported on SiO_2 (Figure S3); Normalized region of bulk Mo_2C

samples carburized at a range of temperatures (Figure S4); LCF fits of bulk Mo_2C samples carburized at a range of temperatures (Figure S5); XRD profiles of bulk Mo_2C samples carburized at a range of temperatures (Figure S6); Rietveld refined patters of the four catalysts prior to testing under RWGS conditions (Figure S7); XRD pattern of Mo_2C/SBA-15-HNC carburized at 923 K (Figure S8); Offline Raman spectra collected of the four catalysts prior to testing under RWGS conditions (Figure S9); XRD profiles post CO_2 activation in reactor (Figure S10); *In situ* XANES spectra on Mo_2C/SBA-15-HNC (Figure S11); *In situ* XANES spectra on Mo_2C/SiO_2-SG (Figure S12); Phase quantification of XANES spectra via LCF (Table S2); LCF fits of Mo_2C supported samples after *in situ* XAS carburization and CO_2 activation (Figure S13); Radial distribution fits of freshly carburized Mo_2C samples *in situ* XAS (Figure S14); XRD spectra of XAS reference materials (Figure S15); Fit parameters of the radial distribution fits of Figure S14 (Table S3); Overview of XRD phase quantification via Rietveld refinement of spent samples (Table S4); Surface area to volume ratio of fresh and spent samples (Table S5).

AUTHOR INFORMATION

Corresponding Author

*E-mail: nico.fischer@uct.ac.za

ORCID

Wijnand Marquart: 0000-0002-7319-0090

Shaine Raseale: 0000-0001-7633-3627

Gonzalo Prieto: 0000-0002-0956-3040

Anna Zimina: 0000-0002-3111-7741

Bidyut Bikash Sarma: 0000-0002-5292-7890

Jan-Dierk Grunwaldt: 0000-0003-3606-0956

Michael Claeys: 0000-0002-5797-5023

Nico Fischer: 0000-0002-8817-3621

Notes

There are no financial conflicts to declare.

ACKNOWLEDGMENTS

All members affiliated with the Catalysis Institute and c*change would like to gratefully acknowledge the financial support received from the DST-NRF Centre of Excellence in Catalysis (c*change) and the University of Cape Town (UCT). We acknowledge Diamond Light Source for time on B18 as part of the Block Allocation Group beamtime of the UK Catalysis Hub in December 2018. A special thanks goes out to R. Cerpath and M. Malatji for their contributions in RWGS catalyst testing as part of their BSc final year project. S. Govender, R. Geland, S. Klink and S. Nyimbinya of the Analytical Laboratory in the Department of Chemical Engineering at UCT for the BET and ICP-OES analysis. M. Jaffer (UCT) for his support with the TEM analysis. M. Waldron for her assistance in the offline Raman analysis. J. Callison and M. Panchal for their assistance in the offline XAS data acquisition. A. Muñoz and I. Lopez (ITQ) are acknowledged for technical assistance with *in situ* Raman studies. We would like to thank the Institute for Beam Physics and Technology (IBPT) for the operation of the storage ring, the Karlsruhe Research Accelerator (KARA).

REFERENCES

(1) Cook, J.; Oreskes, N.; Doran, P. T.; Anderegg, W. R. L.; Verheggen, B.; Maibach, E. W.; Carlton, J. S.; Lewandowsky, S.; Skuce, A. G.; Green, S. A.; Nuccitelli, D.; Jacobs, P.; Richardson, M.; Winkler, B.; Painting, R.; Rice, K. Consensus on Consensus: A Synthesis of Consensus Estimates on Human-Caused Global Warming. *Environ. Res. Lett.* **2016,** *11*, 048002.

(2) Shaftel, H.; Jackson, R.; Callery, S.; Bailey, D. The Causes of Climate Change. https://climate.nasa.gov/ (October 28, 2019).

(3) Zhu, Q. Developments on CO_2-Utilization Technologies. *Clean Energy* **2019,** *3*, 85-100.

(4) Keith, D. W.; Holmes, G.; St. Angelo, D.; Heidel, K. A Process for Capturing CO_2 from the Atmosphere. *Joule* **2018,** *2*, 1573-1594.

(5) Alper, E.; Yuksel Orhan, O. CO_2 Utilization: Developments in Conversion Processes. *Petroleum* **2017,** *3*, 109-126.

(6) *Putting CO_2 to Use - Creating Value from Emissions*; IEA, IEA Publications: Paris, France, 2019.

(7) *Key World Energy Statistics 2019*; IEA, IEA Publications: Paris, France, 2019.

(8) Engineering, C. Carbon Engineering Demonstrates AIR TO FUELS. http://carbonengineering.com/news-updates/ce-demonstrates-air-fuels/ (April 14, 2020).

(9) Linde. Innovative dry reforming process. https://www.linde-engineering.com/en/innovations/innovate-dry-reforming/index.html (April 14, 2020).

(10) Porosoff, M. D.; Yang, X.; Boscoboinik, J. A.; Chen, J. G. Molybdenum Carbide as Alternative Catalysts to Precious Metals for Highly Selective Reduction of CO_2 to Co. *Angew. Chem., Int. Ed. Engl.* **2014,** *53*, 6705-9.

(11) Tsuji, M.; Miyao, T.; Naito, S. Remarkable Support Effect of ZrO_2 upon the CO_2 Reforming of CH_4 over Supported Molybdenum Carbide Catalysts. *Catal. Lett.* **2000,** *69*, 195-198.

(12) Yao, S.; Yan, B.; Jiang, Z.; Liu, Z.; Wu, Q.; Lee, J. H.; Chen, J. G. Combining CO_2 Reduction with Ethane Oxidative Dehydrogenation by Oxygen-Modification of Molybdenum Carbide. *ACS Catal.* **2018,** *8*, 5374-5381.

(13) Zhang, X.; Zhu, X.; Lin, L.; Yao, S.; Zhang, M.; Liu, X.; Wang, X.; Li, Y.-W.; Shi, C.; Ma, D. Highly Dispersed Copper over β-Mo_2C as an Efficient and Stable Catalyst for the Reverse Water Gas Shift (RWGS) Reaction. *ACS Catal.* **2017,** *7*, 912-918.

(14) Amrute, A. P.; Bordoloi, A.; Lucas, N.; Palraj, K.; Halligudi, S. B. Sol–Gel Synthesis of MoO_3/SiO_2 Composite for Catalytic Application in Condensation of Anisole with Paraformaldehyde. *Catal. Lett.* **2008,** *126*, 286-292.

(15) Han, W.; Yuan, P.; Fan, Y.; Liu, H.; Bao, X. Synthesis, Self-Assembly and Disassembly of Mono-Dispersed Mo-Based Inorganic–Organic Hybrid Nanocrystals. *J. Mater. Chem.* **2012,** *22*, 12121-12127.

(16) Wan, C.; Knight, N. A.; Leonard, B. M. Crystal Structure and Morphology Control of Molybdenum Carbide Nanomaterials Synthesized from an Amine-Metal Oxide Composite. *Chem. Commun.* **2013,** *49*, 10409-10411.

(17) Lee, J. S.; Oyama, S. T.; Boudart, M. Molybdenum Carbide Catalysts I. Synthesis of Unsupported Powders. *J. Catal.* **1987,** *106*, 125-133.

(18) Marquart, W.; Morgan, D. J.; Hutchings, G. J.; Claeys, M.; Fischer, N. Oxygenate Formation over K/β-Mo_2C Catalysts in the Fischer–Tropsch Synthesis. *Catal. Sci. Technol.* **2018,** *8*, 3806-3817.

(19) Raseale, S.; Marquart, W.; Jeske, K.; Prieto, G.; Claeys, M.; Fischer, N. Supported Fe_xNi_y Catalysts for the co-Activation of CO_2 and Small Alkanes. *Faraday Discuss.* **2020,** Accepted Manuscript.

(20) Knacke, O.; Kubaschewski, O.; Hesselmann, K. Thermochemical properties of inorganic substances. *Thermochemical properties of inorganic substances*, 2nd ed; Eds.; Springer-Verlag: Berlin, 1991.

(21) Lee, J. S.; Volpe, L.; Ribeiro, F. H.; Boudart, M. Molybdenum Carbide Catalysts II. Topotactic Synthesis of Unsupported Powders. *J. Catal.* **1988,** *112*, 44-53.

(22) Han, W.; Yuan, P.; Fan, Y.; Shi, G.; Liu, H.; Bai, D.; Bao, X. Preparation of Supported Hydrodesulfurization Catalysts with Enhanced Performance using Mo-Based Inorganic–Organic Hybrid Nanocrystals as a Superior Precursor. *J. Mater. Chem.* **2012,** *22*, 25340-25353.

(23) Nair, M. M. High Surface Area Mesoporous Perovskites for Catalytic Applications. PhD, Laval University, Quebec, Canada, 2014.

(24) Rietveld, H. M. A Profile Refinement Method for Nuclear and Magnetic Structures. *J. Appl. Cryst.* **1969,** *2*, 65-71.

(25) Ravel, B.; Newville, M. ATHENA, ARTEMIS, HEPHAESTUS: Data Analysis for X-ray Absorption Spectroscopy using IFEFFIT. *J. Synchrotron Radiat.* **2005,** *12*, 537-541.

(26) Zimina, A.; Dardenne, K.; Denecke, M. A.; Doronkin, D. E.; Huttel, E.; Lichtenberg, H.; Mangold, S.; Pruessmann, T.; Rothe, J.; Spangenberg, T.; Steininger, R.; Vitova, T.; Geckeis, H.; Grunwaldt, J.-D. CAT-ACT—A new highly versatile x-ray spectroscopy beamline for catalysis and radionuclide science at the KIT synchrotron light facility ANKA. *Review of Scientific Instruments* **2017,** *88*, 113113.

(27) Eggart, D.; Zimina, A.; Grunwaldt, J.-D. Manuscript in preparation.

(28) Mo, T.; Xu, J.; Yang, Y.; Li, Y. Effect of Carburization Protocols on Molybdenum Carbide Synthesis and Study on its Performance in CO Hydrogenation. *Catal. Today* **2016,** *261*, 101-115.

(29) Wienold, J.; Jentoft, R. E.; Ressler, T. Structural Investigation of the Thermal Decomposition of Ammonium Heptamolybdate by in situ XAFS and XRD. *Eur. J. Inorg. Chem.* **2003,** *2003*, 1058-1071.

(30) Ovari, L.; Kiss, J.; Farkas, A. P.; Solymosi, F. Surface and Subsurface Oxidation of Mo_2C/Mo(100): Low-Energy Ion-Scattering, Auger Electron, Angle-Resolved X-Ray Photoelectron, and Mass Spectroscopy Studies. *J. Phys. Chem. B* **2005,** *109*, 4638-4645.

(31) Hanif, A.; T., X.; York, A. P. E.; Sloan, J.; Green, M. L. H. Study on the Structure and Formation Mechanism of MoC. *Chemical Materials* **2002,** *14*, 1009-1015.

(32) Liang, P.; Gao, H.; Yao, Z.; Jia, R.; Shi, Y.; Sun, Y.; Fan, Q.; Wang, H. Simple synthesis of ultrasmall β-Mo2C and α-MoC1−x nanoparticles and new insights into their

catalytic mechanisms for dry reforming of methane. *Catalysis Science & Technology* **2017,** *7*, 3312-3324.

(33) Ma, Y.; Guan, G.; Shi, C.; Zhu, A.; Hao, X.; Wang, Z.; Kusakabe, K.; Abudula, A. Low-temperature steam reforming of methanol to produce hydrogen over various metal-doped molybdenum carbide catalysts. *International Journal of Hydrogen Energy* **2014,** *39*, 258-266.

(34) Delporte, P.; Meunier, F.; Phamhuu, C.; Vennegues, P.; Ledoux, M. J.; Guille, J. Physical Characterization of Molybdenum Oxycarbide Catalyst - TEM, XRD and XPS. *Catalysis Today* **1995,** *23*, 251-267.

(35) Scarlett, N. V. Y.; Madsen, I. C. Quantification of phases with partial or no known crystal structures. *Powder Diffraction* **2006,** *21*, 278-284.

(36) Solymosi, F.; Oszko, A.; T.Bansagi; Tolmacsov, P. Adsorption and Reaction of CO2 on Mo2C Catalyst. *Journal of Physical Chemistry B* **2002,** *106*, 9613-9618.

(37) Wan, C.; Regmi, Y. N.; Leonard, B. M. Multiple phases of molybdenum carbide as electrocatalysts for the hydrogen evolution reaction. *Angew Chem Int Ed Engl* **2014,** *53*, 6407-10.

(38) Kurlov, A.; Huang, X.; Deeva, E. B.; Abdala, P. M.; Fedorov, A.; Muller, C. R. Molybdenum carbide and oxycarbide from carbon-supported MoO3 nanosheets: phase evolution and DRM catalytic activity assessed by TEM and in situ XANES/XRD methods. *Nanoscale* **2020,** *12*, 13086-13094.

(39) Kirsch, H.; Sommer, U.; Pfeifer, P.; Dittmeyer, R. Power-to-fuel conversion based on reverse water-gas-shift, Fischer-Tropsch Synthesis and Hydrocracking: Mathematical modeling and simulation in Matlab/Simulink. *Chemical Engineering Science* **2020,** *227*, 115930.

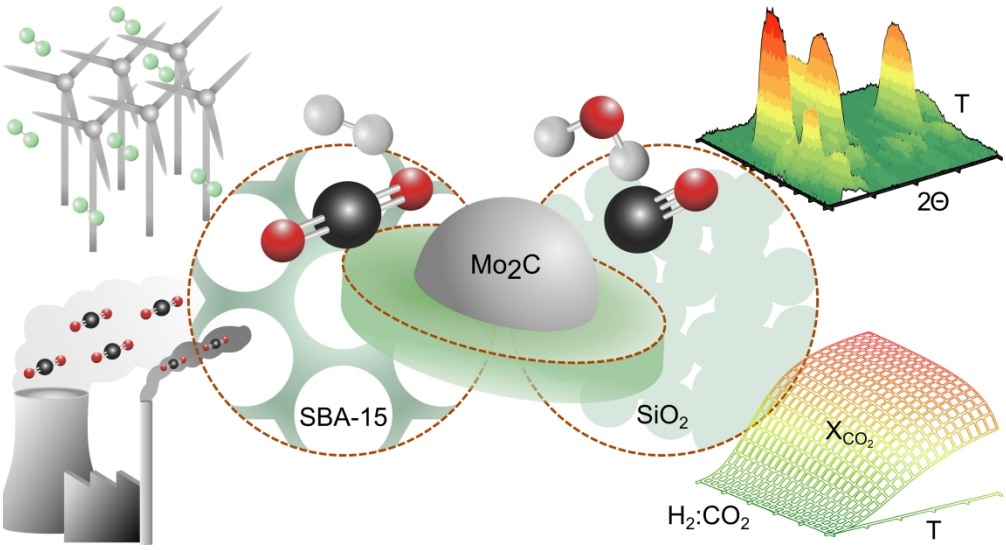

Graphical Abstract